Synthetic Aptamer Mechanoreceptors Enable Cell-Specific Force Sensing and Temporal Control via DNA Circuits

Tao Xu[1], Soumya Sethi[1], Christoph Drees[1], and Andreas Walther[1,2]*

Affiliations

[1] Life-Like Materials and Systems, University of Mainz, Duesbergweg 10-14, Mainz 55128, Germany.

[2] Max Planck Institute for Polymer Research, Ackermannweg 10, 55128 Mainz, Germany.

*Corresponding author. Email: andreas.walther@uni-mainz.de

Abstract

Cells interpret mechanical cues from their microenvironment with spatiotemporal precision to guide adaptive behaviors. However, engineering synthetic mechanosensing systems with both cell-specificity and programmability remains challenging, especially when targeting ubiquitous classical mechanoreceptors. Here, we introduce an all-DNA mechanosensing platform based on aptamers that transmit force through noncanonical surface receptors. Aptamer–receptor recognition acts as a molecular gate for force transduction, enabling the design of mechanoprobes with cell-type selectivity. These probes interpret diverse mechanical inputs via distinct mechanisms, including actomyosin-driven contractility and membrane ruffling during macropinocytosis. By integrating aptamer mechanoprobes with upstream DNA reaction networks, we achieve reversible and temporally programmable mechanoresponses. This modular, all-nucleic-acid system offers a general framework for constructing tunable mechanotransduction circuits. It expands the design space for synthetic mechanobiology and provides new opportunities for autonomous, multi-layered mechanical–biochemical regulation in tissue engineering, morphogenesis, and dynamic cell programming.

Introduction

Mechanical forces are key regulators of cellular behavior, shaping processes from morphogenesis to disease progression by guiding how cells sense, adapt, and respond to their microenvironment.[1–4] These responses are typically mediated by mechanoreceptors, which transduce physical stimuli into biochemical signals controlling cell fate, tissue structure, and homeostasis. Understanding and customizing the mechanotransduction process is pivotal for advancing mechanotargeting-based therapies, tissue engineering, and regenerative medicine.[5,6] However, orchestrating orthogonal cell-specific processes and implementing autonomous control mechanisms during complex morphogenesis is still challenged by the limited specificity, versatility, and dynamic tunability of the current mechanosensing toolbox.[7–9]

Selectivity and differential force sensing at the cellular level are key design principles for engineering synthetic mechanosensing materials. Cells endogenously express a variety of mechanoreceptors including integrins, cadherins, T cell receptors, and Piezo channels to accommodate diverse mechanical demands.[10–13] To engage with those, integrin-targeting mechanoprobes (MPs) have been most widely explored.[14] Pioneering studies have employed DNA-based MPs with Arg-Gly-Asp (RGD) motifs to measure piconewton (pN) forces transmitted through integrins. Depending on the DNA architecture, such probes can provide either irreversible ("historical") readouts via duplex rupture or reversible ("real-time") readouts via hairpin unfolding.[15] Recent innovations have even enabled quantification of single-molecule force loading rates.[16,17] However, the broad and often non-specific expression of integrins across cell types undermines terminal specificity[10,18], limiting their applicability in mixed or heterogeneous cell populations. Greater selectivity can be achieved using protein- or antibody-based ligands conjugated to DNA-MPs, which have proven valuable for interrogating T cell signaling and for constructing mechanosensitive cel-cell junctions.[12,19] In addition to sensing forces, previous DNA MPs have made use of force-induced strand separation to reveal cryptic domains amenable for downstream reactivity, such as in situ dimerization or for ex situ amplification.[20,21] Fully protein-based sensors that mimic Notch signaling offer additional strategies to encode both receptor specificity and force responsiveness, yet these approaches typically require labor-intensive protein engineering, including insertion-site optimization to maintain receptor localization and biological function – thereby limiting accessibility, modularity, and scalability.[22,23]

We hypothesized that aptamers – short single-stranded DNA sequences (ssDNA) selected for high-affinity binding to specific cell surface receptors – could serve as a versatile and new family of synthetic mechanosensors. Unlike classical mechanotransduction targets such as integrins or cadherins, many aptamer-accessible receptors are not canonically associated with force transmission. However, given their roles in signaling, trafficking, and cell migration, and since cells continuously recycle surface proteins for quality control, these receptors may transiently interact with the cytoskeleton or become indirectly coupled to intracellular

force-generating machinery – potentially enabling mechanical engagement through previously unrecognized mechanisms. Indeed, a recent proof-of-concept using the CI-M6PR-targeting aptamer demonstrated that an aptamer can function as a force-reception module to sense weak endocytic forces (~4 pN)[24] and then translate this force cue into intracellular signals via DNA-mediated receptor dimerization.[20] However, that system required soft DNA hairpins suffering from dynamic breathing behavior, which limits force resolution and complicates integration with DNA reaction circuits. More generally, the design space for aptamer-based force sensors remains largely unclear – particularly in terms of cell-type specificity, force thresholding, and mechanistic understanding of how force is generated at the aptamer-receptor interface. Importantly, because aptamers are nucleic acids, they are inherently compatible with DNA-based strand displacement reactions and programmable logic circuits.[25–27] This opens opportunities for dynamic and autonomous regulation of mechanosensing – features that are difficult to achieve with conventional peptide- or protein-based systems like RGD-integrin probes or SynNotch receptors.

Here, we present a modular and fully programmable mechanosensing platform built entirely from nucleic acids, in which DNA aptamers function as synthetic receptor ligands embedded within force-responsive DNA MPs. This approach combines the receptor specificity of aptamers with the tunable force thresholds of DNA mechanics, enabling the systematic exploration of non-canonical and previously unrecognized force-generating surface receptors across diverse cell types. Using this platform, we elucidate the magnitude of noncanonically transmitted forces through DNA MP geometry, and robust cell-type selectivity dictated by aptamer-receptor binding. In contrast to conventional integrin-targeting RGD probes, our aptamer MPs display distinct force transmission behaviors, revealing new mechanistic insights into how specific receptor contexts modulate mechanical engagement. Going further, leveraging the nucleic acid nature of aptamers, we integrate these probes with upstream DNA-based reaction networks to achieve temporal gating and switchable mechanosensitivity. This platform establishes a general framework for constructing adaptive, programmable mechano-interfaces and expands the synthetic biology toolkit for force-guided cell control.

Results

General concept for aptamer-based mechanosensing platform

Our aptamer-based MPs are composed of three modular elements: a terminal aptamer that selectively binds a target receptor, a DNA duplex that acts as a tunable force-sensitive element, and a fluorophore–quencher pair that converts mechanical unfolding into a fluorescence signal (**Fig. 1**). The aptamer functions as a programmable ligand, enabling receptor-specific engagement and ensuring that only receptor-expressing cells generate detectable force signals. To demonstrate the versatility of this platform, we employ five distinct and frequently used aptamers targeting diverse cell-surface receptors across five different cell lines. Moreover, the nucleic acid-based architecture of the aptamer permits dynamic control of receptor recognition via

complementary blocker strands, which can be regulated through DNA-based reaction networks to achieve multi-layered regulatory complexity, such as temporally gated mechanosensing. For surface functionalization, we immobilized biotinylated MPs onto streptavidin-coated glass slides and co-immobilized biotinylated RGD peptides to support baseline integrin-mediated cell adhesion. Supported lipid bilayer-based surface density calibration assays reveal that the densities of different aptamer MPs are in the range of 3500-4500 molecules/μm², and the overall stoichiometric ratio of MPs to RGD is approximately 3:1 (Supplementary Fig. 1, Supplementary Table 2).

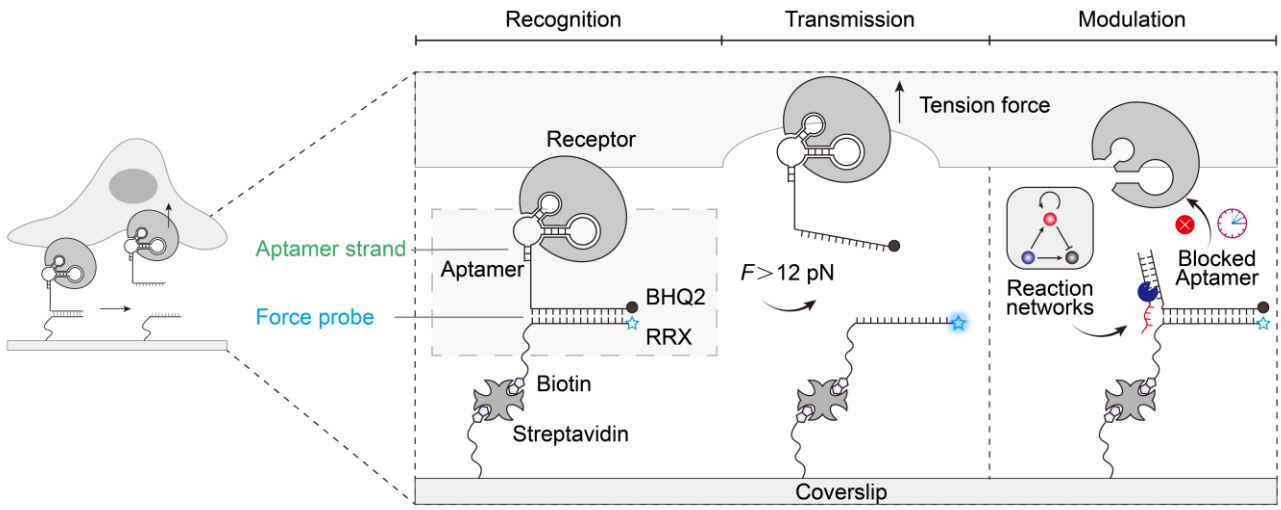

Fig. 1 Aptamer-based mechanoprobes (MPs) enable cell-type-specific mechanosensing and programmable control via upstream DNA reaction networks. The all-nucleic-acid MP consists of a cell-targeting aptamer ligand and a DNA duplex serving as a force sensor. A fluorophore–quencher pair (Rhodamine Red X and BHQ2) transduces mechanical forces into fluorescence signals upon duplex dissociation. Specific force transmission is gated by aptamer–receptor recognition, allowing for cell-type-selective responses. Tuning the geometry of the duplex enables force thresholding to filter defined mechanical inputs. Integration with upstream DNA reaction networks (DRNs) permits programmable and nonlinear regulation of aptamer accessibility, establishing a versatile framework for engineered mechanotransduction.

Force transmission of aptamer MP requires specific aptamer-receptor recognition

To investigate the role of aptamer–receptor recognition in mechanosensing, we designed a MP incorporating the AS1411 aptamer, which binds nucleolin (dissociation constant K_d = 69.1 nM)[28] – a membrane-associated receptor overexpressed in many cancer cells.[29] We selected nucleolin-rich HeLa cells as the test system and used an AS1411 MP with a zipper-type duplex designed to rupture under a low force tolerance (T_{tol}) of 12 pN. Subsequently, we seeded cells onto the MP-functionalized surface and imaged them by total internal reflection fluorescence (TIRF) microscopy after 4 h incubation at 37 °C in 1 % FBS/DMEM medium. Two controls highlight the successful specific activation: One control bears a randomized sequence without affinity to nucleolin, and one lacks any ligand (**Fig. 2**a). As expected, only the AS1411 MP generates significant fluorescence, confirming that specific aptamer-receptor binding enables force transmission (**Fig. 2**a,b). Neither control produces signal, confirming the absence of any nonspecific interactions, such as from dye-membrane interactions (**Fig. 2**b). Interestingly, cell spreading area and cell aspect ratio are similar for the three surfaces (AS1411 MP, random

MP and negative control) within the 4 h observation period, indicating that the AS1411-nucleolin couple does not promote cell adhesion (**Fig. 2**c, Supplementary Fig. 2).

Next, we validate that the AS1411 MP specifically engages the nucleolin receptor by performing colocalization and competitive binding assays. To this end, we employed the TB-5 aptamer[30], which binds to a distinct epitope on nucleolin compared to AS1411, and co-immobilized TB-5and AS1411 MP on the surface at a 1:1 ratio. The mechanosignals from both MPs colocalize, confirming that they both engage nucleolin (**Fig. 2**d). To further confirm specificity, we blocked the AS1411–nucleolin interaction using endostatin, a natural ligand for nucleolin,[29] which reduces the AS1411-derived mechanosignals by 21.7% (**Fig. 2**e). Flow cytometry corroborates this finding, showing a 23.2% decrease in AS1411 binding to HeLa cells in the presence of endostatin (Supplementary Fig. 3). Together, these results demonstrate that force transmission through the AS1411 MP originates from specific aptamer–receptor recognition.

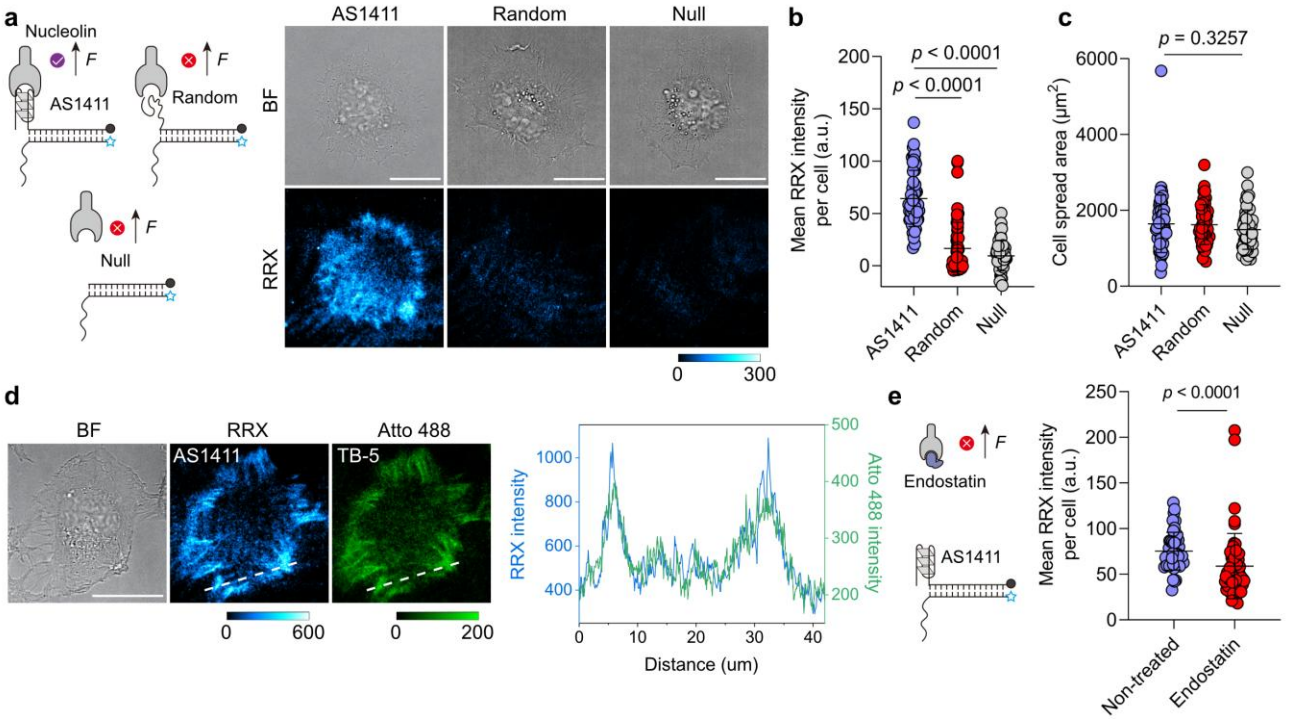

Fig. 2 Specific aptamer–receptor recognition is required for mechanosensing by aptamer-based MPs. a Schematic and representative TIRF images of HeLa cells cultured on surfaces functionalized with AS1411 aptamer, a randomized sequence, or no ligand. **b-c** Quantification of mean fluorescence intensity per cell (**b**) and cell spreading area (**c**) for HeLa cells on each surface. *n* = 54 cells from 3 replicates. **d** Representative brightfield and fluorescence images (TIRF mode) of HeLa cells cultured on surfaces functionalized with a 1:1 ratio of AS1411 and TB-5 MPs. Line profile shows colocalization of AS1411 and TB-5 mechanosignals. **e** Scheme and quantification of mean fluorescence intensity per cell of HeLa cells without and with endostatin blocking (25 µg/mL) on AS1411 MP surfaces. *n* = 45 (control), 54 (blocked) cells from 3 replicates. Statistics (b, c): Kruskal-Wallis test with Dunn's multiple comparisons, (e) Two-tailed, Mann-Whitney test. Scale bars = 20 µm.

Aptamer MPs reveal force magnitudes across noncanonical mechanoreceptors

To compare the force magnitude of aptamer-targeted receptors with common RGD-targeted integrin,[21] we designed each MP with two distinct force geometries. In the unzipping mode, the duplex opens base-by-base,

138 resulting in a low T_{tol} of 12 pN. In contrast, the shearing mode applies force across multiple base pairs near the
139 duplex termini, yielding a higher T_{tol} of 54 pN based on sequence design (**Fig. 3**a).[15]

140 Comparing first both RGD MPs, the RGD-unzipping MP produces markedly stronger fluorescence signals than
141 the RGD-shearing MP, particularly at peripheral focal adhesions (FAs) and at central regions indicative of early-
142 stage adhesion events (**Fig. 3**b). This pattern reflects the lower T_{tol} of the unzipping mode, which enables
143 detection of nascent, low-force adhesion events that fail to activate RGD-shearing MP. Although altering the
144 force geometry modulates the average mechanoresponse pattern per cell (**Fig. 3**c), the overall response based
145 on the integrated intensity remains indistinguishable and independent of the MP geometry (**Fig. 3**d). The
146 integrated intensity reflects the cumulative mechanosignal across the entire cell footprint and is thus not only
147 regulated by intrinsic T_{tol} of the probe but inherently dependent on cell area.[19] This apparent convergence
148 arises because RGD-integrin linkages are capable of transmitting single-molecule forces that exceed both T_{tol}
149 values (>54 pN), and in some cases can even rupture the streptavidin-biotin linkage (> 100 pN).[31] However, the
150 generation of such high forces is contingent on adequate mechanical resistance from the substrate – typically
151 requiring 33-44 pN counterforce to sustain cytoskeletal maturation and stable adhesion.[32] As a result, shearing-
152 mode MPs promote cell spreading and increase overall force generation, thereby blurring the difference in
153 integrated mechanoresponse between both geometries (**Fig. 3**e).[19]

154 In contrast, AS1411 MPs show a pronounced distinction between unzipping and shearing geometry. The
155 unzipping mode consistently produces stronger signals in both mean and integrated intensity (**Fig. 3**b-d). Two
156 factors account for this behavior: First, the AS1411-nucleolin couple transmits substantially lower force
157 (consistently below 54 pN) than RGD-integrin engagement. Second, unlike integrins, the AS1411-nucleolin pair
158 alone does not promote cell spreading (**Fig. 2**c, and **Fig. 3**e). This property makes the shearing mode of aptamer
159 MPs particularly well-suited for tandem integration with other DNA nanodevices,[33,34] where mechanical
160 stability is essential to avoid unintended force-induced detachment.

161 Since the above results suggest that aptamers cannot promote cell adhesion, it raises the question to what
162 extent baseline adhesion is required for aptamer MPs to function. To address this, we prepared surfaces
163 functionalized solely with aptamer MPs without co-immobilized RGD to investigate mechanosensing under
164 minimal adhesion conditions. HeLa cells are largely unable to spread on surfaces presenting AS1411 MPs alone,
165 regardless of whether unzipping or shearing MPs are used (**Fig. 3**f). Compared with RGD co-immobilized
166 conditions, AS1411 unzipping-mediated mechanosignals are significantly reduced to below 24.4 % (**Fig. 3g**),
167 implying that baseline cell adhesion is a prerequisite for AS1411-based force sensing.

168 Considering that we aim to develop receptor-orthogonal aptamer MPs, we further investigated the Sgc8-
169 aptamer as a potential MP for the protein tyrosine kinase 7 (PTK7), using HepG2 cells that overexpress this
170 receptor. Interestingly, Sgc8 MPs-functionalized surfaces exhibit a somewhat different behavior (**Fig. 3**h). Even

171 though Sgc8 MPs alone also fail to promote HepG2 cell spreading, robust mechanoactivation occurs (**Fig. 3**i).
172 Even in a non-spread, quasi-suspended state (see brightfield images), HepG2 cells effectively activate Sgc8
173 unzipping MPs, yielding ring-like mechanosignals. This indicates that for Sgc8-PTK7, baseline cell adhesion is
174 not a prerequisite for mechanoactivation. The differential adhesion dependence of these two aptamer MPs
175 suggests that they transmit forces through fundamentally distinct mechanisms, which we will further discuss
176 below.

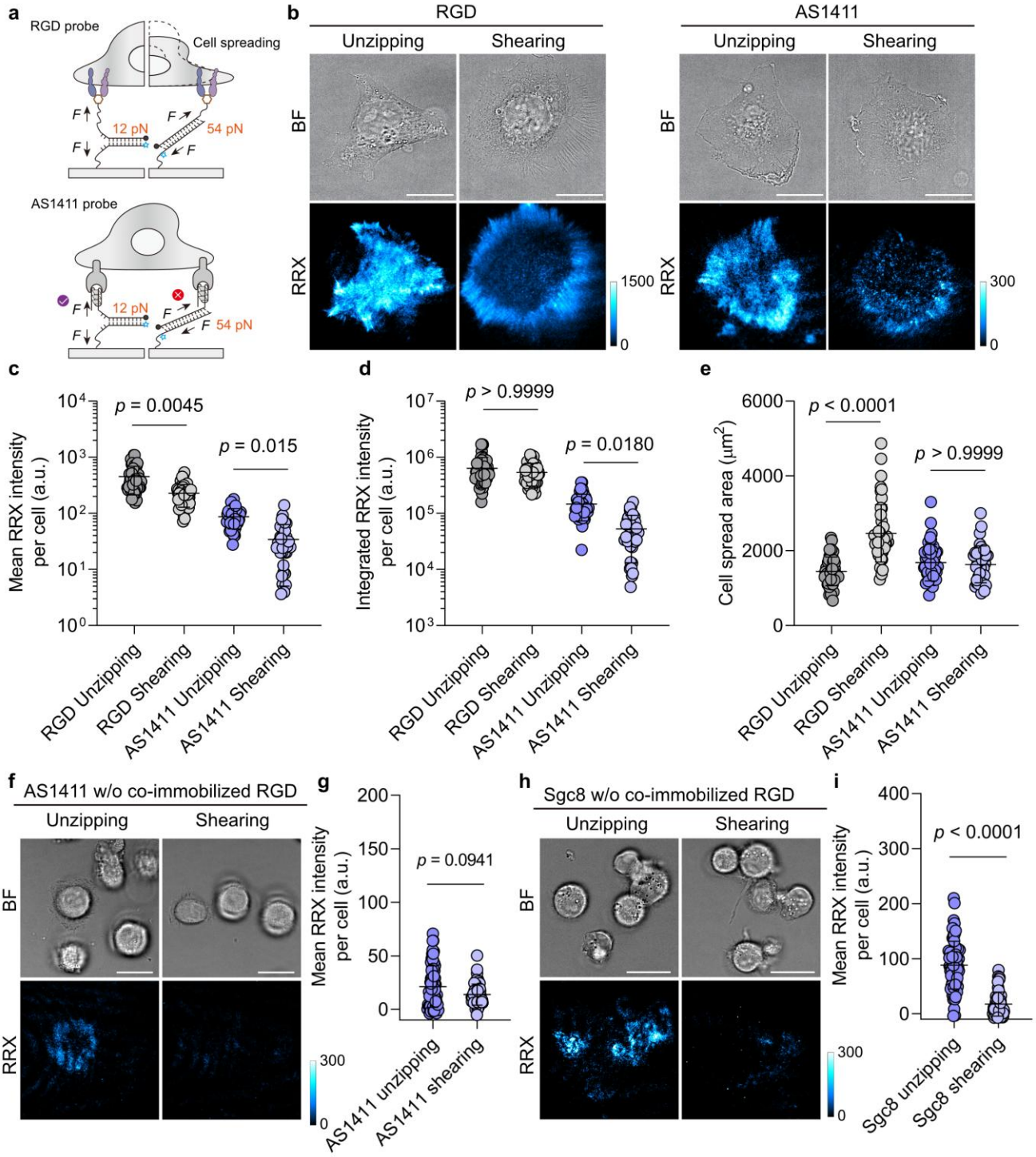

Fig. 3 Aptamer MPs reveal force magnitudes across noncanonical mechanoreceptors. a Scheme of the mechanosensing through unzipping and shearing geometries in RGD and AS1411 MPs. **b** Representative brightfield and fluorescence images of HeLa cells cultured on surfaces functionalized with RGD or AS1411 MPs featuring different force geometries. **c-e** Quantification of (**c**) mean fluorescence intensity per cell, (**d**) integrated fluorescence intensity per cell, and (**e**) cell spreading area for HeLa cells on each MP type and geometry. n = 49, 47, 45, 36 (left to right) cells from 3 replicates. Statistics: Kruskal-Wallis test with Dunn's multiple comparisons. Note that both mean and integrated intensity are shown because mean intensity mainly captures the T_{tol}-dependent shifts while integrated intensity is cross-regulated by both the intrinsic T_{tol} of the probe and the cell spreading area. **f** Representative brightfield and fluorescence images of HeLa cells cultured on surfaces functionalized with AS1411 MPs alone featuring different force geometries. No co-immobilized RGD-biotin is present to support baseline cell adhesion. Most HeLa cells remain non-adherent and fail to activate the unzipping AS1411 MPs. Only few cells adhering to the surface via nonspecific interactions can activate MPs. **g** Quantification of mean fluorescence intensity per cell for HeLa cells on each geometry. n = 68, 67 cells from 3 replicates. Statistics: Two-tailed, Mann-Whitney test. **h** Representative brightfield and fluorescence images of HepG2 cells cultured on surfaces functionalized with Sgc8 MPs alone

featuring different force geometries. No co-immobilized RGD-biotin is present to support baseline cell adhesion. Non-spread HepG2 cells activate Sgc8 MPs. **i** Quantification of mean fluorescence intensity per cell for HepG2 cells on each geometry. *n* = 71, 68 cells from 3 replicates. Statistics: Two-tailed, Mann-Whitney test. Scale bars = 20 µm

Source of forces associated with noncanonical mechanoreceptors

Although nucleolin is a well-established molecular target,[35,36] it has not been previously associated with the exertion of mechanical force on the extracellular environment. Our data reveal distinct differences to integrin-targeting MPs, prompting us to investigate the source of nucleolin-associated forces. To test whether aptamer-receptor internalization contributes to force generation, we treated HeLa cells with pathway-specific inhibitors. Neither chlorpromazine (CPZ, 28 µM), which inhibits clathrin-mediated internalization,[37] nor methyl-β-cyclodextrin (MβCD, 1.9 mM) which inhibits caveolin- and lipid-raft-mediated uptake,[38] alters the mechanosignal intensity (**Fig. 4**a, b). In contrast, treatment with 5-(N-ethyl-N-isopropyl) amiloride (EIPA, 100 µM), an inhibitor of macropinocytosis,[39] reduces mechanosignals by 29.8 % (**Fig. 4**b). This implicates macropinocytosis in the mechanoactivation of the AS1411 MP, consistent with previous findings that cancer cells take up free AS1411 aptamers predominantly via macropinocytosis.[40] Flow cytometry further supports this conclusion, showing a 76.6 % reduction in the uptake of free AS1411 aptamers by HeLa cells in the presence of EIPA (Supplementary Fig. 4). Notably, compared to the free state in solution, the inhibitory effect of EIPA decreases by 46 % when AS1411 is immobilized as a MP on a surface. These results suggest that while macropinocytosis contributes to force generation, it may not be the main source of nucleolin-mediated force.

Interestingly, previous studies reported molecular associations between nucleolin and multiple focal adhesion-related or cytoskeletal components, including integrins $\alpha_v\beta_3$,[41] $\alpha_5\beta_1$,[42] and β_1,[43] focal adhesion protein talin,[44] and myosin heavy chain 9.[45] To determine whether nucleolin-mediated forces spatially correlate with FA structures, we transfected HeLa cells with a plasmid for constitutive expression of monomeric enhanced green fluorescent protein (mEGFP)-paxillin and visualized the actin cytoskeleton with phalloidin staining. Notably, nucleolin-generated forces are clearly localized at peripheral FA sites marked by paxillin, suggesting a spatial and functional association between nucleolin and FAs (**Fig. 4**c, d, Supplementary Fig. 5). Based on this, we hypothesized nucleolin may indirectly couple to the actomyosin cytoskeleton to transmit mechanical force (**Fig. 4**e). To identify the cytoskeletal components responsible for this transmission, we treated cells with specific inhibitors after allowing 30 min of initial adhesion.[16,46] Inhibiting actin polymerization with cytochalasin D (10 µM) moderately reduces mechanosignals by 38.9 % (**Fig. 4**f, Supplementary Fig. 6). In contrast, blocking myosin II ATPase activity with blebbistatin (25 µM) causes a pronounced 77.5 % decrease. Together, these results demonstrate that nucleolin-mediated forces primarily depend on myosin-driven contractility, which may be relayed through FAs or other physical linkages independently coupled to the actomyosin network before reaching nucleolin.

To understand the differential dependence of Sgc8 aptamer MPs on baseline adhesion (see above, **Fig. 3**f,h),

224 we investigated the underlying source of Sgc8-PTK7 forces. Unlike the FA-like patterns observed for nucleolin,
225 PTK7-activated mechanosignals display spatially distinct, ring-like force patterns with submicron size (**Fig. 4**g).
226 Those are consistent with a macropinocytic origin, as clathrin- and caveolin-mediated internalization typically
227 generates vesicles in the nanometer range.[47] To test this hypothesis, we inhibited macropinocytosis using EIPA
228 (100 μM), which substantially reduces mechanoactivation by 51.9 %, whereas CPZ (28 μM) and MβCD (1.9 mM)
229 inhibiting clathrin- and caveolin-mediated endocytosis have no effect (**Fig. 4**g, h, Supplementary Fig. 7). To
230 further examine the spatial organization of these signals, we stained the plasma membrane and performed
231 TIRF microscopy. As expected, the ring-like mechanofluorescence predominantly localizes to the peripheries
232 of dark membrane invaginations, consistent with force generation during membrane ruffling in early-stage
233 macropinocytosis (**Fig. 4**i, j, Supplementary Fig. 8).[48]

234 To understand the cytoskeletal origin of this force generation, we next examined the roles of actin
235 polymerization and myosin action during different macropinocytic phases. Actin polymerization is critical for
236 driving membrane ruffling and protrusion formation during the early-stage macropinocytosis, whereas
237 myosins contribute to actin network contraction at the base of ruffles as the membrane closes to form
238 macropinosomes.[49] Treatment with cytochalasin D (10 μM, actin polymerization inhibitor) and blebbistatin (25
239 μM, myosin II inhibitor) reduces mechanosignals by 56.1 % and 32.6 %, respectively, suggesting that force
240 generation is dominated by actin polymerization rather than myosin-driven contraction (**Fig. 4**k,
241 Supplementary Fig. 9). Phosphoinositide 3-kinase (PI3K) catalyzes membrane sealing by generating PIP_3 at the
242 ruffle bases, thereby recruiting effectors for actin remodeling and vesicle closure.[50] While PI3K activity is
243 essential for membrane sealing, it is dispensable for ruffle formation.[51] Consistent with this, inhibition of PI3K
244 using LY294002 (50 μM) does not affect mechanosignals, further confirming that PTK7-mediated forces
245 originate primarily from early-stage membrane ruffling during macropinocytosis with minimal contribution
246 from the sealing phase (**Fig. 4**l,m).

247 To further distinguish between two force transmission mechanisms, we knocked down the orthogonal
248 regulator neuronal Wiskott-Aldrich syndrome protein (N-WASP). As a critical cytoskeletal regulator, N-WASP
249 interacts with Arp2/3 complex to drive branched actin polymerization,[52] thereby regulating essential cellular
250 processes such as membrane ruffling, endocytosis, and cytoskeletal remodeling. Inhibition of the Arp2/3
251 complex has been shown to inhibit Arp2/3-mediated actin polymerization in phagocytic adhesion rings of
252 macrophages but have little effect on integrin-mediated tensions in FAs.[53] The latter depends on myosin II-
253 loaded stress fibers which lack Arp2/3 complex. For the AS1411-nucleolin pair, compared with cells transfected
254 with scrambled siRNA, N-WASP knockdown HeLa cells still exhibit a stripe-like force pattern, although the signal
255 amplitude is reduced by 27.9% (**Fig. 4**n, Supplementary Fig. 10a). This result indicates that force transmission
256 through the AS1411-nucleolin pair is weakly dependent on N-WASP. In contrast, for the Sgc8-PTK7 pair, N-

WASP knockdown in HepG2 cells leads to an almost complete loss of the ring-like pattern, with a 57.8% reduction in signal intensity relative to scrambled controls, suggesting a strong dependence on N-WASP-mediated actin dynamics (**Fig. 4**o, Supplementary Fig. 10b). Moreover, the different effects of N-WASP knockdown in both cell lines closely mirror the results observed upon EIPA treatment (**Fig. 4**b,h). This is consistent with the fact that EIPA inhibits Rac1/Cdc42 activity, and Cdc42 is a key upstream activator of N-WASP.[54] Together, these results demonstrate that the AS1411-nucleolin and Sgc8-PTK7 pairs exhibit distinct dependencies on N-WASP and downstream Arp2/3-mediated branched actin polymerization, reflecting fundamentally different force transmission pathways.

Source of nucleolin-mediated force

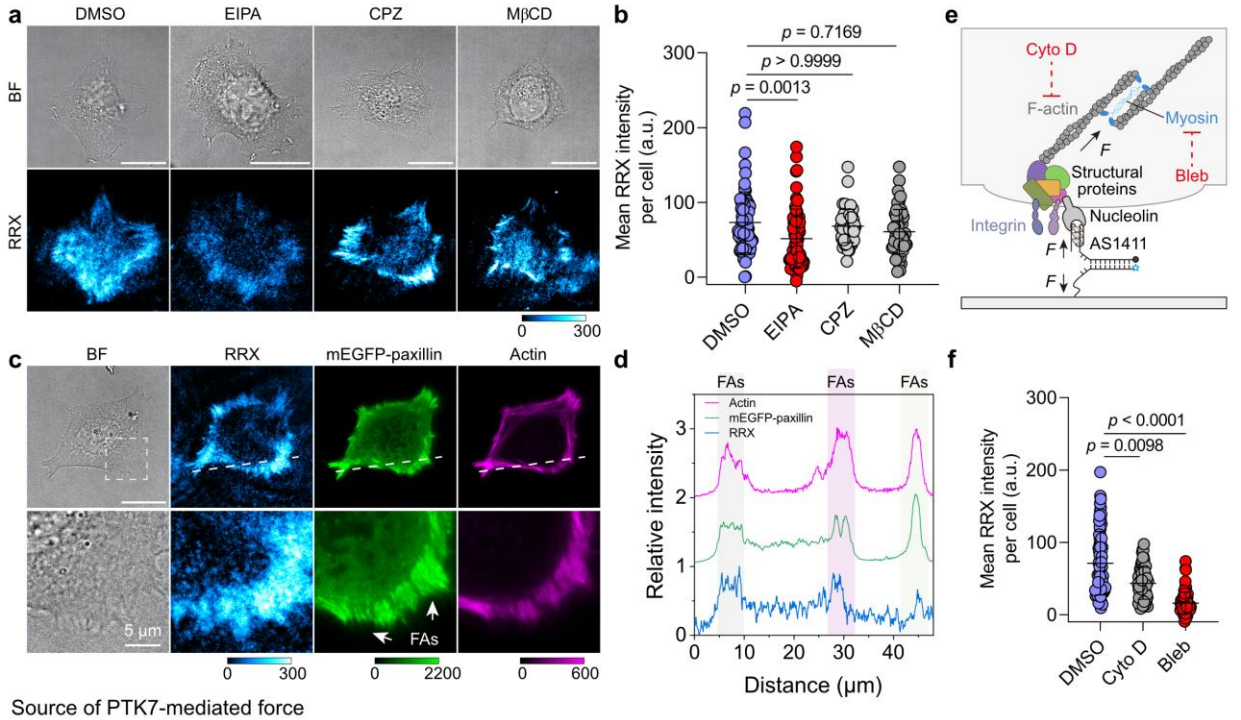

Source of PTK7-mediated force

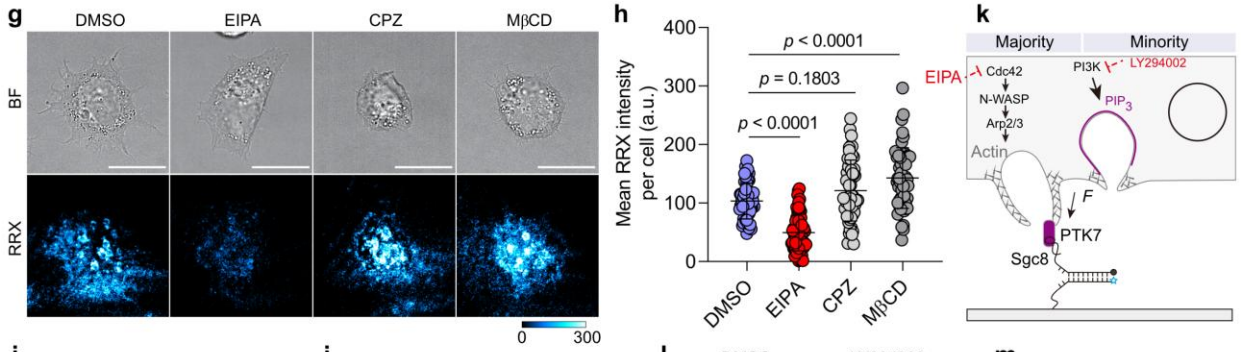

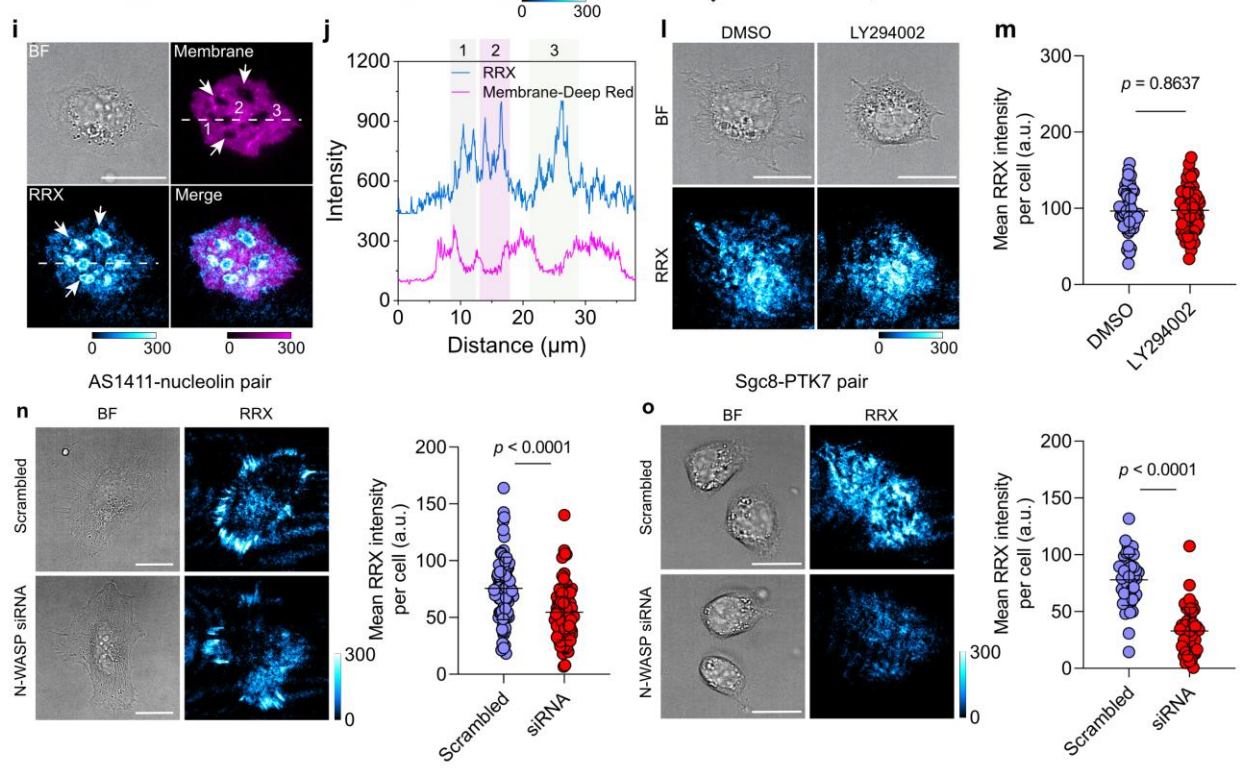

265

Fig. 4 Aptamer MPs reveal force origins associated with noncanonical mechanoreceptors. a Representative brightfield and fluorescence images of HeLa cells treated with internalization inhibitors on AS1411 MP surfaces. **b** Quantification of mean fluorescence intensity per cell for HeLa cells under the indicated conditions. *n* = 70, 70, 54, 54 (left to right) cells from 3 replicates. Statistics: Kruskal-Wallis test with Dunn's multiple comparisons. **c** Representative images of HeLa cells on AS1411 MP surfaces showing brightfield, mechanosignal, mEGFP-paxillin, and phalloidin-stained actin. **d** Line profile along the white line in (c) shows intensity profiles of mechanosignals, mEGFP-paxillin, and actin. **e** Schematic: forces acting on nucleolin arise from myosin-II-driven contractility. **f** Quantification of mean fluorescence intensity per cell following cytoskeletal inhibitor treatment. *n* = 72 cells from 3 replicates. Statistics: Kruskal-Wallis test with Dunn's multiple comparisons. **g** Representative brightfield and fluorescent images of HepG2 cells treated with internalization inhibitors on Sgc8 MP surfaces. **h** Corresponding quantification of mean fluorescence intensity per cell. *n* = 54 cells from 3 replicates. Statistics: One-way ANOVA with Bonferroni post-hoc tests. **i** Representative images showing plasma membrane staining, mechanosignals and brightfield of HepG2 cells incubated on Sgc8 MP surfaces. **j** Line profile from (i) reveals spatial colocalization of mechanosignals at the inner edge of membrane invaginations. **k** Schematic: PTK7-mediated forces originate from actin polymerization/membrane ruffling during early-stage macropinocytosis; membrane sealing contributes minimally. **l** Brightfield and fluorescence images of HepG2 cells treated with PI3K inhibitor LY294002 on Sgc8 MP surfaces. **m** Quantification of mean fluorescence intensity per cell for HepG2 cells without and with LY294002 treatment on Sgc8 MP surfaces. *n* = 54 cells from 3 replicates. Statistics: Unpaired, two-tailed student's *t*-test. **n-o** Effect of N-WASP on nucleolin- and PTK7-mediated force. **n** Representative brightfield and fluorescence images of HeLa cells after N-WASP siRNA knockdown on AS1411 MP surfaces. Mean fluorescence intensity per cell was quantified. n = 85, 83 cells from 3 replicates for scrambled and siRNA groups. Statistics: unpaired two-tailed Student's *t*-test. **o** Representative brightfield and fluorescence images of HepG2 cells after N-WASP siRNA knockdown on Sgc8 MP surfaces. Mean fluorescence intensity per cell was quantified. n = 45 cells from 3 replicates. Statistics: unpaired two-tailed Student's *t*-test. Scale bar = 20 μm.

Versatility of aptamer MPs to customize cell-type-specific mechanoresponses

The specificity of aptamer-receptor recognition enables the modular customization of MPs for cell-type-specific mechanosensing. We demonstrate this principle using three aptamer MPs – Sgc8, MUC1 S2.2 and SYL3c – which target PTK7 (K_d = 0.85 nM)[55], mucin-1 (K_d = 0.12 nM)[56], and epithelial cell adhesion molecule (EpCAM, K_d = 38 nM)[57], respectively. We tested each MP on both receptor-high-expressing and receptor-low-expressing cell lines, selected based on differential receptor expression profiles confirmed by flow cytometry (Supplementary Fig. 11). Mucin-1-high-expressing HeLa cells strongly activate the MUC1 S2.2 MP, whereas HepG2 cells with substantially lower levels of mucin-1 show minimal response (**Fig. 5**a,b). Conversely, HeLa cells fail to activate the SYL3c MP due to low EpCAM receptor levels. This contrasts with EpCAM-high-expressing MDA-MB-231 cells (**Fig. 5**c,d). Similarly, HepG2 cells generate stronger activation of the Sgc8 MP than A549 cells, consistent with their higher PTK7 expression (**Fig. 5**e,f). Interestingly, beyond expression level-dependent signal magnitude, different cell types expressing the same receptor can exhibit distinct, cell-type-dependent force patterns. HeLa cells express PTK7 at an intermediate level (Supplementary Fig. 11e,f). Mechanosensing using Sgc8 MPs reveals a stripe-like force pattern in contrast to the characteristic ring-like mechanosignals observed in HepG2 cells (**Fig. 5**e,f). These results indicate that different cell types may transmit forces through the same receptor via distinct pathways, a phenomenon that cannot be inferred from receptor expression levels alone. Collectively, the high differential selectivity of aptamer-receptor MP pairs highlights the broad adaptability of our platform for sensing mechanoresponses across diverse cell types and receptor classes.

Motivated by the need for selective and precise mechanoresponse in complex multicellular environments, we extend our validation beyond simple single-cell-type systems. To this end, we labeled receptor-high-expressing and receptor-low-expressing cells with CellTrace Deep Red and Violet dyes, respectively, and co-seeded them

in wells containing the corresponding aptamer MPs to assess cell-type-specific mechanoresponse (**Fig. 5**g). Indeed, mechanoactivation of the Sgc8 MP occurs exclusively in the Deep Red-labeled PTK7-high-expressing HepG2 cells, while the Violet-labeled PTK7-low-expressing A549 cells exhibit much lower signals (**Fig. 5**h,i). Switching to the MUC1 S2.2 MP leads to strong mechanosignals in the Deep Red-labeled mucin-1-high-expressing HeLa cells, whereas Violet-labeled mucin-1-low-expressing HepG2 cells show minimal signals (**Fig. 5**j,k). These results underscore the utility of aptamer MPs as customizable mechanical elements for precise, cell-type-specific mechanochemical transduction in heterogeneous cell populations.

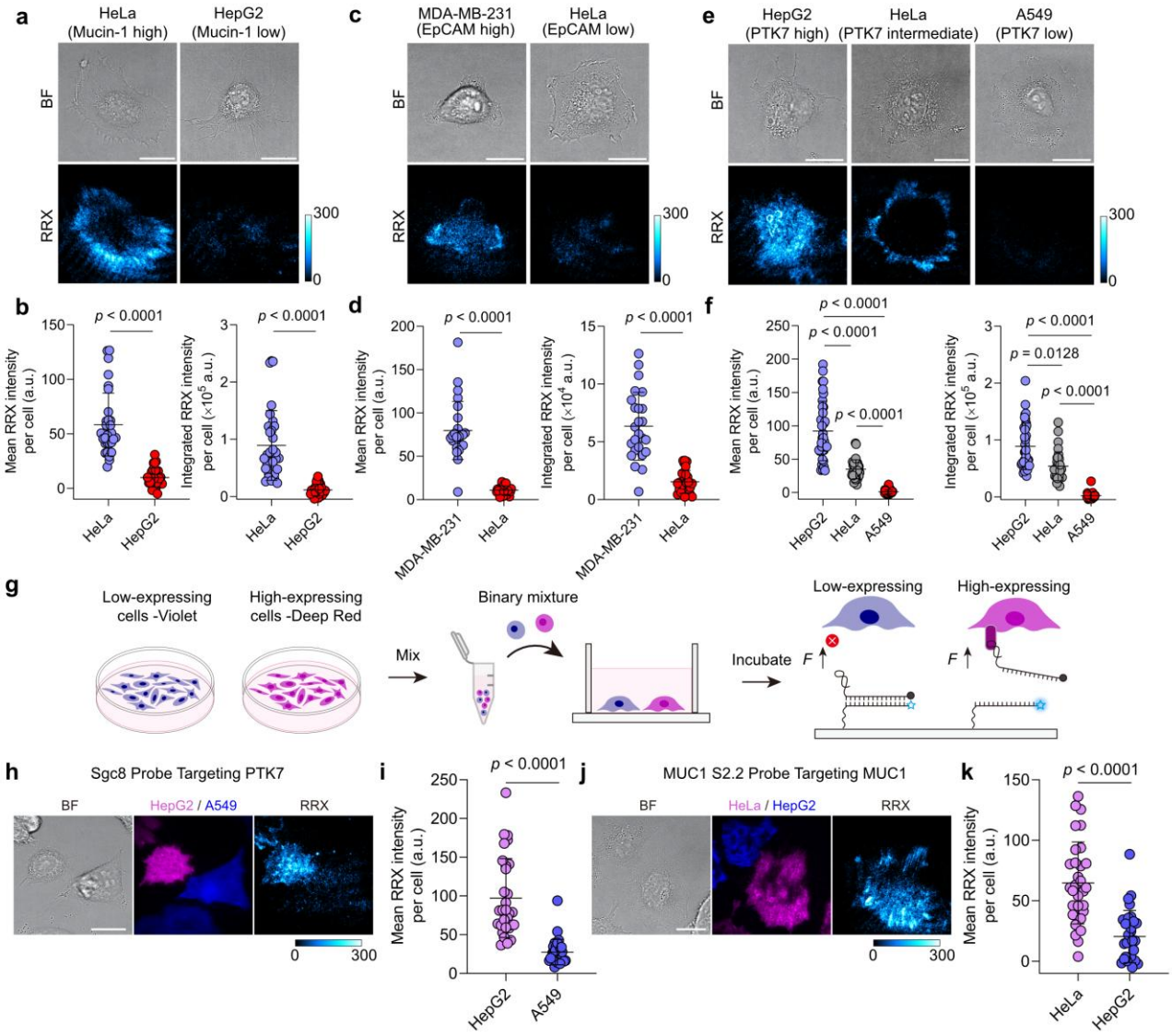

Fig. 5 Customized cell-type-specific mechanoactivation enabled by aptamer-receptor recognition. a Representative images of HeLa (mucin-1-high-expressing) and HepG2 (mucin-1-low-expressing) cells on MUC1 S2.2 MP surfaces. **b** Corresponding quantification of mean and integrated fluorescence intensity per cell of HeLa and HepG2 cells on MUC1 S2.2 MP surfaces. n = 31, 27 cells from 3 replicates. Statistics: Two-tailed, Mann-Whitney test. Note that both mean and integrated intensity are shown here because different cell lines may have distinct basal morphologies with different cell area. **c** Representative images of MDA-MB-231 (EpCAM-high-expressing) and HeLa (EpCAM-low-expressing) cells on SYL3c MP surfaces. **d** Corresponding quantification of mean and integrated fluorescence intensity per cell of MDA-MB-231 and HeLa cells on SYL3c MP surfaces. n = 25, 27 cells from 3 replicates. Statistics: Two-tailed, Mann-Whitney test. **e** Representative brightfield and fluorescence images of HepG2 (PTK7-high-expressing), HeLa (PTK7-intermediate-expressing) and A549 (PTK7-low-expressing) cells on Sgc8 MP surfaces. **f** Corresponding quantification of mean and

integrated fluorescence intensity per cell of HepG2, HeLa and A549 cells on Sgc8 MP surfaces. *n* = 36, 31, 27 cells from 3 replicates. Statistics: Kruskal-Wallis test with Dunn's multiple comparisons. **g** Schematic of co-culture assay design. Receptor-high-expressing and -low-expressing cells were pre-labeled with CellTrace Deep Red and Violet dyes, respectively, mixed 1:1, and co-seeded onto aptamer MP-functionalized surfaces. **h** Representative images of HepG2 (PTK7-high-expressing, Deep Red) and A549 (PTK7-low-expressing, Violet) cells co-cultured on Sgc8 MP surfaces. **i** Quantification of mechanosignals in HepG2 vs A549 cells. n = 30 cells from 3 replicates. Statistics: Two-tailed, Mann-Whitney test. **j** Representative images of co-cultured HeLa (mucin-1-high-expressing, Deep Red) and HepG2 (mucin-1-low-expressing, Violet) cells on MUC1 S2.2 MP surfaces. **k** Corresponding quantification of mechanosignals as mean fluorescence intensity per cell. *n* = 31 cells from 3 replicates. Statistics: Unpaired, two-tailed student's *t*-test. Scale bars = 20 µm.

Aptamer MPs enable programmable mechanoresponses via integration with DNA-based reaction networks (DRNs)

Natural mechanotransduction involves temporally orchestrated biochemical signals that guide adaptive cellular responses. Aptamers, unlike protein or peptide ligands, offer the unique advantage that their DNA structure can be seamlessly integrated with DRNs to emulate this dynamic regulation. Importantly, aptamers can be manipulated directly at their binding site with DRNs without detaching them from the underlying surface by for instance breaking the force-sensitive duplex, thus ensuring their correct configuration and integrity.

To introduce temporal control over mechanoactivation, we regulate aptamer accessibility using designer blocker and activator strands that can be designed with tunable affinities based on base-pairing principles (**Fig. 6**a). We first use a blocker fully complementary to AS1411 to completely prevent binding to nucleolin. This blocker also contains a 5-nucleotide (nt) toehold, enabling its subsequent removal via a toehold-mediated strand displacement reaction (SDR) triggered by an activator strand. In this design, mechanoactivation becomes conditional on the possibility for aptamer-receptor engagement, which can be dynamically regulated through SDR. Cell-free surface assays confirm robust and reversible aptamer blocking (Supplementary Fig. 12). The blocker quenches >90 % of a fluorescently labeled, surface-tethered AS1411 aptamer within 30 min, indicating effective blocking. Subsequent medium exchange with the equimolar DNA activator restores ~ 50 % of the signal within 30 min with a reaction rate of 2.14×10^{-2} min^{-1}, confirming aptamer reactivation (see Methods, Supplementary Fig. 12a-d, Supplementary Table 3). We next validate this mechanism under live-cell conditions for two consecutive suppression-recovery cycles. In the first cycle, adding 200 nM blocker 30 min after seeding suppresses AS1411-nucleolin mechanoactivation by 75.1 %. Subsequent medium exchange with 200 nM activator restores 82.5 % of the original signal, consistent with aptamer re-engagement and functional recovery of mechanosensing (**Fig. 6**b). The second blocker-activator cycle closely mirrors the suppression-recovery behavior observed in the initial cycle (Supplementary Fig. 12e). The overall higher signal level can be attributed to cumulative mechanoactivation accumulated during the additional activation period

Going a step beyond external switching, we next introduce more advanced enzyme-catalyzed DRNs upstream of mechanoactivation to autonomously program the temporal accessibility of aptamer MPs.[26,27] To this end, we replace the DNA blocker with an RNA analogue. This RNA blocker can be selectively degraded by RNase H

362 only when bonded as RNA-DNA duplex at the MP. This degradation releases the aptamer and restores
363 mechanoactivation within programmable time windows (**Fig. 6**c). In this context, RNase H acts as a biochemical
364 gatekeeper. Additional temporal control can be gained by introducing freely diffusing RNA-DNA duplexes as
365 decoy substrates, which compete with the RNA-blocked MP for RNase H activity.

366 The kinetics of the timer circuit for MP activation depend on the DRN parameters. First, the RNase H
367 concentration can be used to control the time for mechanoactivation to occur. Monitoring the aptamer
368 reconfiguration kinetics with simple fluorescence assays reveals RNase H concentration-dependent reaction
369 rates of 0.71 $\times 10^{-2}$ min^{-1} at 10 U/mL and 5.26 $\times 10^{-2}$ min^{-1} at 100 U/mL (see Methods, Supplementary Fig. 13a,
370 Supplementary Table 3). When it comes to force sensing, low RNase H concentrations (≤1 U/ml) fail to initiate
371 measurable mechanoresponse within 4 h. At 10 U/mL, mechanoactivation is restored to 78.2%, while
372 100 U/mL yields near-complete recovery, consistent with efficient RNA blocker degradation (**Fig. 6**d,e). To
373 further tune the system, we then fixed RNase H at 10 U/mL and introduced the RNA-DNA decoy (**Fig. 6**f). The
374 introduction of decoy strand exerts a clear, dose-dependent inhibitory effect on the reaction rate of RNA
375 blocker degradation (Supplementary Fig. 13b, Supplementary Table 3). Consistent with this trend, 10 nM
376 decoy is sufficient to slightly delay the mechanoresponse, whereas 100 nM nearly abolishes the response
377 within 4 h and a significant response is observed only at 7 h (**Fig. 6**g,h, Supplementary Fig. 13c).

378 Because RNA-RNaseH modules can be extended into more complex signaling DRNs,[25] our aptamer
379 manipulation strategy opens doors for more complex temporal programs in the future. We note that similar
380 programmable mechanoactivation could also be achieved using antibody- or nanobody-based probes that
381 block receptor access via engineered protein blockers and activator with progressively tuned affinities.
382 However, such protein-based systems would require extensive efforts, including site-directed mutagenesis,
383 affinity optimization, and computational modeling to fine-tune the underlying protein–protein interactions. In
384 contrast, aptamer systems offer a far more accessible and modular alternative, leveraging predictable base-
385 pairing rules to design dynamic, multistage mechanical response circuits in a straightforward manner.

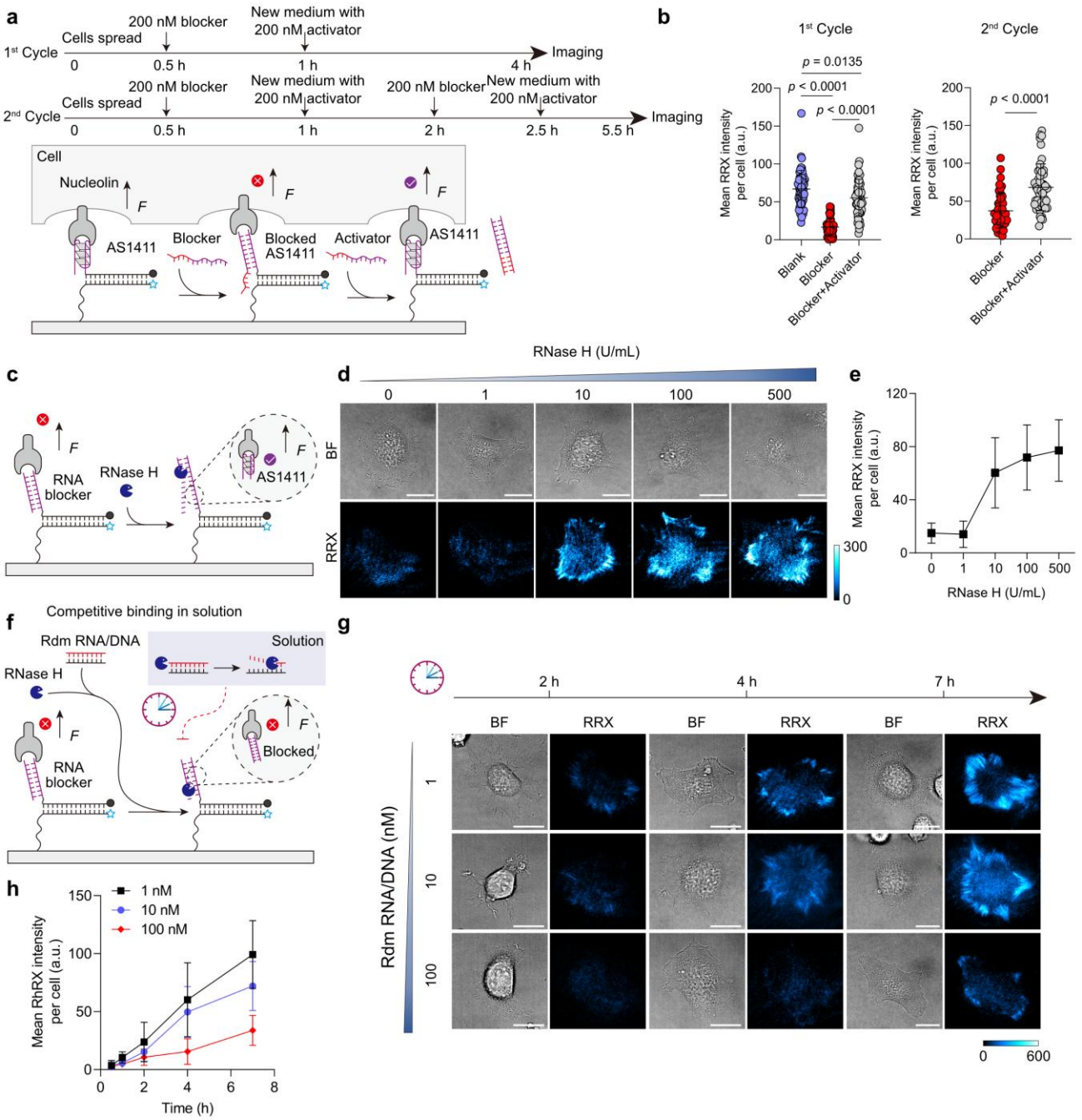

Fig. 6 Programmable mechanoactiovation enabled by upstream DRNs. a Schematic of switchable mechanosensing using SDRs for two suppression-recovery cycles. In the 1st cycle, HeLa cells were seeded on surfaces grafted with AS1411 MP for 30 min, followed by addition of 200 nM DNA blocker strands to inhibit aptamer-receptor interaction. After another 30 min, 200 nM DNA activator strands were introduced to displace the blockers via toehold-mediated SDR, restoring mechanosensing. Mechanosiganls were quantified after 3 h. In the 2nd cycle, another round of blocker strands was introduced 1 h after adding activator strands in the 1st cycle. After an additional 30 min, a second-round activator was introduced. Consistent with the 1st cycle, the system was incubated for 3 h prior to imaging. **b** Quantification of mean fluorescence intensity per cell of HeLa cells on AS1411 MP surfaces after sequential blocker and activator treatment for two suppression-recovery cycles. 1st cycle, n = 54 cells from 3 replicates. 2nd cycle, n = 48 cells from 3 replicates. Statistics: 1st cycle, One-way ANOVA with Bonferroni post-hoc tests. 2nd cycle, Two-tailed, Mann-Whitney test. **c** Schematic of enzyme-catalyzed mechanoactivation. Aptamer MPs are initially blocked by complementary RNA strands. Addition of RNase H at varying concentration (0-500 U/mL) degrades the RNA in the RNA–DNA duplexes, resetting the aptamer configuration and restoring mechanosensing. Cells were imaged after 4 h of incubation. **d** Representative brightfield and fluorescence images of HeLa cells on RNA-blocked AS1411 MP surfaces following addition of different RNase H concentrations. **e** Corresponding quantification of mean fluorescence intensity per cell. *n* = 36 cells from 3 replicates. **f** Schematic of delayed mechanoactivation. Aptamer MPs are RNA-blocked and exposed to 10 U/mL RNase H. Increasing concentrations of freely diffusing RNA–DNA decoy duplexes (1–100 nM) compete for RNase H activity, thereby delaying aptamer reactivation. **g** Representative brightfield and fluorescence images of HeLa cells on RNA-

blocked AS1411 MP surfaces after adding 10 U/mL RNase H and varying RNA/DNA duplex concentrations. **h** Corresponding quantification of mean fluorescence intensity per cell. Reaction medium: 1 % FBS, 1 % P/S, 100 μg/mL actin protein, DMEM. *n* = 27 cells from 3 replicates. Scale bars = 20 μm.

Conclusion

We have introduced aptamer-based MPs as a specific, modular, and programmable platform for mechanosensing that enables customizable mechanoresponses with cell-type selectivity. We find that aptamer–receptor recognition is a critical determinant of specific force transmission. Exploiting distinct receptor expression profiles on different cells, it is now possible to engineer cell-type-specific mechanoresponses that filter irrelevant mechanical stimuli and facilitate precise functional specialization. Such capabilities are essential for constructing complex behaviors in multicellular systems.

To contextualize the advantages of aptamer MPs, it is instructive to compare them with conventional ligand–receptor systems commonly used in mechanobiology. Although high-affinity ligands such as cRGDfK can achieve targeted, force-responsive delivery of therapeutic agents (e.g., anticancer drugs or antisense oligonucleotides) across $\alpha_v\beta_3$-positive cells,[34,58] their promiscuity toward various integrin subtypes and the structural similarity among integrins limit specificity.[18] Moreover, RGD-integrin engagement promotes adhesion reinforcement, which blurs discrimination between different force geometries. In contrast, aptamers, as shown for the Sgc8-PTK7 interaction, can be functionally decoupled from adhesion processes, rendering the tension tolerance (T_{tol}) a dominant parameter in mechanoactivation. This enables the use of aptamer MPs as force-selective mechanical gates and allows their modular integration with other DNA-based nanodevices.

The excellent selectivity of aptamer MPs underscores their importance to interpret noncanonical mechanoreceptors outside of the classical mechanobiology realm. On the molecular level, we have elucidated two distinct force transmission behaviors: nucleolin-mediated forces arise from actomyosin contractility, whereas PTK7-mediated forces originate from membrane ruffling/actin polymerization during early-stage macropinocytosis. These two cases are not meant to be exhaustive but rather exemplify that noncanonical mechanoreceptors can engage in mechanical signaling via diverse, receptor-specific pathways. By proposing a systematic framework for receptor-specific mechanosensing, we lay the groundwork for future exploration of alternative mechanotransduction pathways. These newly uncovered mechanisms also expand the potential of aptamers as versatile force-reception modules for bidirectional mechano-biochemical signal transduction. Beyond relying on weak DNA hairpins to sense clathrin-mediated endocytic forces (~4 pN),[20] cells can exert forces >12 pN on aptamer MPs. Such forces allow the irreversible exposure of cryptic ssDNA domains that can trigger downstream reactions such as transcription, hairpin chain reactions,[21] or rolling circle amplification.[59] This expanded force range substantially broadens the design space for intelligent, force-responsive material interfaces capable of cellular adaptation.

The identification of noncanonical forces highlight the importance of revisiting the biological functions of both

437 these aptamers and receptors from a mechanobiological perspective. Determining whether these receptors
438 are directly coupled to classical adhesion structures or are independently linked to the same actomyosin
439 network via intermediary components will be essential for uncovering more general principles. Whether
440 similar interactions occur under native conditions remains to be elucidated. A prime candidate is the precursor
441 of the nucleolin ligand endostatin, located in the NC1 domain of type XVIII collagen,[60] which may serve as a
442 native anchor for nucleolin despite potential differences in binding affinity. Addressing these questions could
443 reveal how cryptic motifs within the ECM regulate cellular homeostasis through non-canonical
444 mechanotransduction pathways. Meanwhile, caution is required when extrapolating from aptamer-receptor
445 pairs to native ligand-receptor interaction, particularly regarding the immobilization state of the ligand, binding
446 affinity and bond mechanics, and the multivalency and cooperative effects inherent to native ligands. For
447 example, the AS1411 aptamer binds nucleolin with a K_d of 69.1 nM,[28] which is lower than that of its native
448 ligand endostatin (23.2 nM),[61] suggesting that our measurements may slightly underestimate the native
449 capacity for tension generation. Finally, the generalizability of the aptamer-based platform provides
450 opportunities to probe other established aptamer-receptor pairs with well-defined biological functions, such
451 as PD-L1-targeting aptamers involved in immune checkpoint regulation,[62,63] or CD28 costimulatory aptamers
452 in T cells,[64] to determine whether their biological activities are similarly regulated by mechanical force.

453 The all-nucleic-acid nature of aptamer MPs offers unique advantages by enabling seamless integration with
454 the broader toolbox of DNA nanotechnology. Without detaching MPs (or ligands), we introduced two modes
455 of precise upstream control over receptor engagement: Reversible switching via SDR and programmable timing
456 via RNase H–driven DRNs. Unlike protein- or nanobody-based MPs, this programmability requires no protein
457 engineering, expression, or purification, but only base-pairing logic. This molecular tunability allows
458 mechanotransduction to transcend simple linear outputs and adopt complex, nonlinear, and time-resolved
459 behaviors. Such temporal precision is especially vital in biological systems, such as morphogenesis and
460 embryonic development, where cells interpret mechanical and biochemical signals in tightly orchestrated
461 spatiotemporal patterns.[7] Moving forward, pioneering work using protein-ligand functionalized MPs has
462 shown that strand displacement can control intracellular mechanics in 3D spheroids,[65] although at the cost of
463 ligand release. Introducing aptamer-based MPs further enables non-invasive, tunable modulation without
464 compromising probe integrity. However, long-term application in these environments still faces stability
465 challenges. While modifications like peptide nucleic acids,[66] phosphorothioate linkages,[67] or our recent L-DNA
466 strategy protect the MP structure,[68] single-stranded aptamers remain inherently degradation-prone. Balancing
467 their structural integrity with binding affinity is critical. In this context, using nuclease inhibitors such as actin
468 or decoy DNA may be more effective.[69,70] Additionally, for potential *in vivo* applications, deep-tissue diffusion,
469 off-target effects arising from protein corona formation, and potential immunotoxicity remain significant
470 challenges.

471 Looking to the future, aptamer MPs could be further expanded by incorporating an upstream biochemical
472 control layer responsive to endogenous signals, ranging from small molecules (e.g., ions, ATP), to proteins
473 (e.g., cytokines), to even specific cell types.[71] Acting as a molecular bridge, aptamer MPs can transduce force
474 into the exposure of cryptic ssDNA sites, which in turn can initiate localized signal amplification, recruit
475 biomolecular effectors, modulate synthetic receptors, and ultimately trigger feedback-regulated mechanical
476 circuits within or across cells. We envision that such aptamer-based, programmable, and feedback-coupled
477 mechano-adaptive systems could accelerate the development of cell-autonomous behaviors, guide adaptive
478 morphogenetic processes, and provide a foundation for future advances in synthetic biology and tissue
479 engineering.

480 **Methods**

481 **Materials**

482 Hydrogen peroxide (35 %), sulfuric acid (95 %), (3-Aminopropyl)triethoxysilane (APTES), phosphate buffered
483 saline (PBS) and ethanol were purchased from Carl Roth. Biotin-PEG-NHS 5K (HE041023-5K) was purchased
484 from Biopharma. 5(6)-(Biotinamidohexanoylamido)pentylthioureidylfluorescein was purchased from
485 BLDpharm. Cyclo[Arg-Gly-Asp-d-Phe-Lys(PEG-PEG-azide)] (RGD-3759-PI), and Cyclo[Arg-Gly-Asp-D-Phe-
486 Lys(Biotin)] (cRGD-Biotin, PCI-3895-PI) were purchased from Biosynth. 25 mm x 75 mm glass coverslips (10812),
487 and sticky slide 8 well (80828) were purchased from ibidi. All oligonucleotides were purchased from Biomers.
488 1,2-Dioleoyl-sn-glycero-3-phosphocholine (DOPC), 5-(N-ethyl-N-isopropyl) amiloride, chlorpromazine
489 hydrochloride, Methyl-β-cyclodextrin, LY 294002, Cytochalasin D and Blebbistati were purchased from Sigma-
490 Aldrich. Streptavidin (434302), Alexa Fluor Plus 405 Phalloidin (A30104), CellTrace violet cell profileration kit
491 (C34571), CellTrace far red cell proliferation kit (C34564), bovine albumin fraction V (BSA, 7.5% solution),
492 paraformaldehyde solution (4% in PBS),anti-PTK7 monoclonal antibody (MA5-25774), Alexa Fluor 488 anti-
493 CD227 (Mucin-1) monoclonal antibody (53-9893-82), Alexa Fluor 488 anti-CD326 (EpCAM) monoclonal
494 antibody (53-8326-42), Alexa Fluor 488 goat anti-mouse IgG (H+L) cross-adsorbed secondary antibody (A-
495 11001), Alexa Fluor™ 647 goat anti-mouse IgG (H+L) highly cross-adsorbed secondary antibody (A-21236),
496 Texas Red™ 1,2-Dihexadecanoyl-sn-Glycerin-3-Phosphoethanolamin, Triethylammoniumsalz (Texas Red™
497 DHPE), and Oregon Green™ 488 1,2-Dihexadecanoyl-*sn*-Glycerin-3-Phosphoethanolamin (Oregon Green™ 488
498 DHPE) were purchased from Thermo Fisher Scientific. N-WASP antibody (C-1, sc-271484) was purchased from
499 Santa Cruz. RNase H was purchased from New England Biolabs. Actin protein (>95% pure, rabbit skeletal muscle)
500 was purchased from Cytoskeleton, Inc. All buffers were prepared with nuclease free water. All chemicals and
501 enzymes were used as such without any further purification.

502 **DNA Hybridization**

503 DNA concentrations were determined using a DeNovix-S-06873 (DeNovix OS 0.8.1 v4.1.5) spectrophotometer.
504 DNA oligonucleotides were hybridized at 10 µM in a TE buffer additionally containing 12.5 mM $MgCl_2$ in 200
505 µL PCR tubes and subsequently diluted to 125 nM. DNA oligonucleotides were heated to 95 °C and then cooled
506 at a rate of 1.3 °C/min to 25 °C.

507 **Surface preparation**

508 Surface preparation method was modified from previously published protocols.[21] Briefly, glass coverslips (25 x
509 75 mm) were rinsed with ultrapure water and sequentially sonicated in water and ethanol for 20 min each.
510 The coverslips were then immersed in freshly prepared piranha solution (3:1 v/v concentrated sulfuric acid
511 (95 %) to hydrogen peroxide (30 %)) for 1 h. **Caution:** Piranha solution becomes very hot upon mixing, and is
512 highly oxidizing and may explode upon contact with organic solvents. Then, the coverslips were washed 6 times
513 with ultrapure water, followed by 4 successive ethanol washes. For amine functionalization, the coverslips were
514 incubated in 3 % v/v APTES at room temperature for 1 h. The coverslips were then washed 6 times with ethanol,
515 and baked at 80 °C for 20 min. Slides were then reacted with Biotin-PEG-NHS (1 % w/v) for 1 h in ultrapure
516 water. Next, the coverslips were washed 3 times with ultrapure water, dried under N_2 gas, and stored at -80°C
517 until use.

518 The biotinylated coverslips were adhered to sticky-slide 8-well chambers. Wells were incubated with 50 µg/mL
519 of streptavidin for 1 h at room temperature, followed by three washes with nuclease-free water. Wells were
520 then incubated with 200 µL of 250 nM probe solution (125 nM cRGD-biotin and 125 nM DNA probes) for 1 h
521 at room temperature. After washing with nuclease free water, cell imaging media (1 % FBS, 1 % P/S, DMEM;
522 see below) was added to the well followed by the addition of cells.

523 **Probe Density Calibration**

524 **Lipid vesicles.** Lipid vesicles were prepared with 100% 1,2-Dioleoyl-sn-glycero-3-phosphocholine (DOPC) or
525 with 99.5mol% DOPC and 0.5mol% Texas Red DHPE (TR-DHPE) or Oregon Green™ 488 DHPE (OG-DHPE). Lipid
526 was dissolved in chloroform in a round-bottom glass tube and then carefully dried with a nitrogen stream while
527 rotating the tube. The films were then placed in vacuum for 2 h for complete evaporation of the solvent and
528 stored at -20°C until further use. Small unilamellar vesicles (SUVs) were formed by sonicating the lipids in
529 nanopure water, with a lipid concentration of 2 mg/mL. The dried lipids were resuspended in Nanopure water
530 at 2 mg/ml by sonicating. To generate small unilamellar vesicles (SUVs), lipids were then extruded 20 times
531 through a mini-extruder (Avanti Research 610000-1EA) assembled with a 0.1 µm polycarbonate membrane.

532 **Solution phase standard curve preparation.** To relate dye brightness, the brightness of known concentrations
533 of labeled oligonucleotides and SUVs were measured in solution.[72] A glass bottom 96-well plate was first
534 washed with ethanol and water and passivated with 1% BSA for 1h to prevent any surface adsorption. Different

535 concentrations of labeled oligonucleotides and SUVs (0-800 nM) were then added to each well and their bulk
536 fluorescence intensity in solution was measured with a fluorescence microscope (20x objective lens) to create
537 a standard curve. The scaling factor *F* factor was defined as:

$$F = \frac{Slope_{labeled\ oligonucleotides}}{Slope_{labeled\ SUVs}} \quad (1)$$

538 where $Slope_{labeled\ oligonucleotides}$ and $Slope_{labeled\ SUVs}$ represent the slopes of the plots of fluorescence intensity versus
539 concentration for the labeled oligonucleotides and SUVs, respectively.

540 **Supported lipid bilayer preparation.** A glass-bottom 96-well plate was used for preparing supported lipid
541 bilayers.[21,34] Each well was filled and soaked with ethanol for 15 min and rinsed with nuclease free water.
542 Subsequently, 200 µL of 6 M NaOH solution was added to each well for base etching at room temperature for
543 1 h. After washing each well with Nanopure water, lipid mixtures containing different percentage of labeled
544 SUVs (0, 0.01, 0.05, 0.1, 0.25, 0.5 mol.%) were added at 0.5 mg/mL in PBS with 2.5 mM calcium ions (100 µL)
545 to coat the glass surfaces for 20 min. After the lipid vesicles fused to the surfaces, the wells were rinsed with
546 PBS and imaged with a fluorescence microscope to create a standard curve for probe density. Note that the
547 substrate should never come in contact with air, as this will damage the supported membrane.

548 **Cell culture and transfection**

549 HeLa (ACC 57) and HepG2 (ACC 180) were purchased from DSMZ. A549 (DSMZ, ACC 107) and MDA-MB-231
550 (DSMZ, ACC 732) were gifts from Tanja Weil laboratory at Max Planck Institute for Polymer Research. HeLa cells
551 were cultured in Minimum Essential Medium (MEM) (10 % fetal bovine serum (FBS), 1% penicillin–
552 streptomycin (P/S)) at 37 °C with 5 % CO_2. A549 and MDA-MB-231 cells were cultured in Dulbecco's Modified
553 Eagle Medium (DMEM) (10 % FBS, 1 % P/S) at 37 °C with 5 % CO_2. HepG2 cells were cultured in RPMI 1640
554 Medium (10 % FBS, 1 % P/S) at 37 °C with 5 % CO_2. mEGFP-paxillin WT plasmid was a gift from Michael Rosen
555 (Addgene plasmid # 186152).[73] Transfection was carried out using the Lipofectamine 3000 Transfection
556 Reagent (Invitrogen, L3000015) following the manufacturer's instructions. N-WASP knockdown was carried out
557 using human N-WASP siRNA (Santa Cruz, sc-36006) or control siRNA-A (Santa Cruz, sc-37007) with
558 Lipofectamine RNAiMAX Transfection Reagent (Invitrogen, 13778030) following the manufacturer's
559 instructions.

560 **Force imaging, image acquisition and analysis**

561 All cells were seeded onto the MP surfaces in cell imaging medium (1% FBS, 1% P/S, DMEM) and incubated at
562 37 °C with 5 % CO2 for 4 h, except for Figs. 6h-i, where incubation times were 2, 4, and 7 h. TIRF and brightfield
563 microscopy were performed on a Zeiss Elyra 7 Imaging System equipped with 405 nm, 488 nm, 561 nm, and
564 642 nm excitation lasers using alpha Plan-Apochromat 63x, N.A. 1.46.oil immersion, TIRF objective, pco.edge

565 4.2 CLHS water-cooled sCMOS cameras. Live cell imaging was conducted at 37 °C in humidified air with 5 %
566 CO_2. Microscopy experiments were typically conducted using the following parameters: 405 nm laser: 0.4 %
567 output (~0.01 mW), 488 nm laser: 0.8 % output (~0.7 mW), 561 nm laser: 0.8 % output (~0.8 mW) and 642 nm
568 laser: 0.4 % output (~0.4 mW). Beam splitters (primary, secondary): LBF 405/488/561/642, SBS BP 490-560 +
569 LP 640. Exposure time: 50 ms (except for Fig. 2d, RRX-AS1411 200 ms, Atto488-TB-5 200 ms; Fig. 5h, A549-
570 Violet 200 ms; Fig. 5j, HeLa-Deep Red 100 ms, HepG2-Violet 200 ms). TIRF angle: 66° (n_{oil}: 1.518). All images
571 were contrasted equally.

572 Background subtraction methods were adapted from previously published protocols.[68] Briefly raw images were
573 exported to FIJI (software) followed by selecting 3 ROIs in the fluorescent channel, next the background
574 intensity was measured and subtracted from the images.

575 Immunofluorescence staining of N-WASP was imaged by confocal laser scanning microscopy (CLSM) using a
576 Leica Stellaris 5 microscope (LasX v4.3.0.24308) with four laser lines and three HyD S detectors using plan-
577 apochromat objec6ves (63×, 1.40 numerical aperture, oil immersion).

578 **Inhibition experiments**

579 100 µM 5-(N-ethyl-N-isopropyl) amiloride (EIPA), 1.9 mM Methyl-β-cyclodextrin (MβCD), 28 µM
580 chlorpromazine hydrochloride (CPZ) were used to inhibit the macropinocytosis, caveolae and clathrin-
581 mediated internalization, respectively. 50 µM LY 294002 was used to inhibit the PI3K. 10 µM cytochalasin D
582 and 25 µM Blebbistatin were used to inhibit the actin polymerization and myosin ATPase, respectively.

583 **Immunostaining**

584 Cells were fixed with 4 % (w/v) paraformaldehyde in PBS for 15 min at room temperature and permeabilized
585 with 0.25 % (v/v) Triton X-100 in PBS for 10 min, followed by washes in PBS twice. Unspecific binding was
586 blocked using 10 % normal goat serum in PBS for 30 min at room temperature. After removing blocking solution,
587 cells were incubated with anti N-WASP primary antibody (1:25 dilution) at 4 °C overnight. After rinsing three
588 times with PBS, cells were incubated in secondary antibody (1:500 dilution) and Hoechst 34580 (1:200 dilution)
589 in 1% BSA for 1 h at room temperature. For actin staining, fixed cells were incubated with Alexa Fluo Plus 405
590 Phalloidin (1:200 dilution) in 2.5 % (w/v) BSA/PBS at room temperature for 1 h. Samples were then washed
591 three times in PBS for 5 min each before microscopic observations.

592 **Flow cytometry**

593 To assess the competitive binding of endostatin to nucleolin, 5×10^5 cells were incubated with 25 µg/mL
594 endostatin and 2.5 µM FAM-AS1411 in 3 % (w/v) BSA/PBS at 4 °C for 60 min. Cells were washed and then
595 resuspended in PBS before running through flow cytometer. To quantify the receptor expression levels, 5×10^5

596 cells were labelled with fluorescent primary antibodies (Alexa Fluor™ 488-anti-MUC1: 5 µg/mL, Alexa Fluor™
597 488-anti-EpCAM: 5 µg/mL) in 3 % (w/v) BSA/PBS at 4 °C for 30 min. For labelling PTK7, cells were incubated
598 with primary antibody anti-PTK7 (2 µg/mL) in 3 % (w/v) BSA/PBS at 4 °C for 30 min. Cells were washed three
599 times with PBS and then incubated in Alexa Fluor™ 488-secondary antibody (5 µg/mL) in 3 % (w/v) BSA/PBS at
600 37 °C for 30 min. After labelling, cells were washed and resuspended in PBS. To assess the effect of EIPA on
601 AS1411 internalization, 2×10^5 cells were seeded in standard cell medium in 12-well plates and incubated
602 overnight at 37 °C. Cells were then incubated with 100 µM EIPA and 500 nM FAM-AS1411 in 1 % FBS/DMEM
603 at 37 °C for 4 h. Cells were washed and then resuspended in PBS before running through flow cytometer.

604 Flow cytometry experiments were performed on a Novocyte Quanteon (Agilent, NovoExpress v.1.6.0) with 4
605 excitation lasers (violet 405 nm, blue 488 nm, yellow-green 561 nm and red 640 nm) and 16 fluorescence
606 detectors. A total of 10,000 events were collected per sample. Flow cytometry data was analyzed using
607 FLOWJO (v10.8.1) software.

608 **Statistical analysis**

609 Each experiment was performed at least three independent times. Statistical results were analyzed using
610 GraphPad Prism 8.0 and shown as the mean ± s.d. Comparisons between two groups were conducted using
611 unpaired two-tailed Student's t-test (Figs. 4m and 5k), and among three or more groups using one-way ANOVA
612 with Bonferroni test correction (Figs. 4h and 6b) as indicated. If a data set did not pass the normality tests, the
613 significances were calculated with Mann-Whitney (Figs. 2e, 3g, 3i, 5b, 5d, 5i, and 6b) for two-group
614 comparisons or Kruskal-Wallis corrected with Dunn's test (Figs. 2b-c, 3c-e, 4b, 4f, and 5f) for multiple groups.
615 For all analyses, *P < 0.05, **P < 0.01 and ***P < 0.001, ****P < 0.0001 were considered significant. NS
616 indicates statistical non-significance with $P > 0.05$.

617 **Acknowledgments**

618 We would like to thank Dr. Siyu Song and Dr. Miao Xie for their helpful discussion about cell experiments. We
619 thank Dr. Marcos Masukawa for his help with the preparation of supported lipid bilayers. We acknowledge IMB
620 Flow Cytometry Core Facility for the flow cytometry data acquisition. This project has received funding from
621 the European Research Council (ERC) under the European Union's Horizon 2020 research and innovation
622 program (M3ALI:101001638), as well as from the CoM2Life start-up funds of JGU.
623 T. X. acknowledges support from the Max Planck Graduate Center. A. W. acknowledges funding via a Gutenberg
624 Research Professorship and a Max Planck Fellowship underpinning his Life-Like Materials Program. The Zeiss
625 Elyra 7 was funded by the Gutenberg Research College and Deutsche Forschungsgemeinschaft (DFG;
626 497845157). Open Access funding enabled and organized by Projekt DEAL.

627 **Author Contributions**

T.X. and A.W. conceived the project. T.X. designed, performed all the experiments, and conducted data analysis. S.S. helped with the surface preparation and probe immobilization. C.D. helped with TIRF measurement. T.X., S.S. C.D. and A.W. discussed the data. T.X. and A.W. wrote the manuscript with input from all authors. A.W. supervised the project.

Competing interests

The authors declare no conflict of interest.

Data availability

All data are available in the article and its Supplementary Information are available from the corresponding author upon reasonable request.

Supplementary Information

Supplementary information is available in the online version of the paper.

Reference

1. Vining, K. H. & Mooney, D. J. Mechanical forces direct stem cell behaviour in development and regeneration. *Nat. Rev. Mol. Cell Biol.* **18**, 728–742 (2017).
2. Iskratsch, T., Wolfenson, H. & Sheetz, M. P. Appreciating force and shape — the rise of mechanotransduction in cell biology. *Nat. Rev. Mol. Cell Biol.* **15**, 825–833 (2014).
3. Van Helvert, S., Storm, C. & Friedl, P. Mechanoreciprocity in cell migration. *Nat. Cell. Biol.* **20**, 8–20 (2018).
4. Chaudhuri, O., Cooper-White, J., Janmey, P. A., Mooney, D. J. & Shenoy, V. B. Effects of extracellular matrix viscoelasticity on cellular behaviour. *Nature* **584**, 535–546 (2020).
5. Huebsch, N. *et al.* Harnessing traction-mediated manipulation of the cell/matrix interface to control stem-cell fate. *Nat. Mater.* **9**, 518–526 (2010).
6. Kim, S., Uroz, M., Bays, J. L. & Chen, C. S. Harnessing mechanobiology for tissue engineering. *Dev. Cell* **56**, 180–191 (2021).
7. Negrete, J. & Oates, A. C. Towards a physical understanding of developmental patterning. *Nat. Rev. Genet.* **22**, 518–531 (2021).
8. Toettcher, J. E., Voigt, C. A., Weiner, O. D. & Lim, W. A. The promise of optogenetics in cell biology: interrogating molecular circuits in space and time. *Nat. Methods* **8**, 35–38 (2011).
9. Seo, D. *et al.* A mechanogenetic toolkit for interrogating cell signaling in space and time. *Cell* **165**, 1507–1518 (2016).
10. Kechagia, J. Z., Ivaska, J. & Roca-Cusachs, P. Integrins as biomechanical sensors of the microenvironment. *Nat. Rev. Mol. Cell Biol.* **20**, 457–473 (2019).
11. De Belly, H., Paluch, E. K. & Chalut, K. J. Interplay between mechanics and signalling in regulating cell fate. *Nat. Rev. Mol. Cell Biol.* **23**, 465–480 (2022).
12. Hu, Y. *et al.* Quantifying T cell receptor mechanics at membrane junctions using DNA origami tension sensors. *Nat. Nanotechnol.* **19**, 1674–1685 (2024).
13. Xiao, B. Mechanisms of mechanotransduction and physiological roles of PIEZO channels. *Nat. Rev. Mol. Cell Biol.* **25**, 886–903 (2024).
14. Wang, X. & Ha, T. Defining single molecular forces required to activate integrin and notch signaling. *Science* **340**, 991–994 (2013).
15. Hu, Y., Duan, Y. & Salaita, K. DNA nanotechnology for investigating mechanical signaling in the immune

system. *Angew. Chem. Int. Ed.* **62**, e202302967 (2023).
16. Jo, M. H. *et al.* Determination of single-molecule loading rate during mechanotransduction in cell adhesion. *Science* **383**, 1374–1379 (2024).
17. Hu, Y. *et al.* DNA-based ForceChrono probes for deciphering single-molecule force dynamics in living cells. *Cell* **187**, 3445-3459.e15 (2024).
18. Slack, R. J., Macdonald, S. J. F., Roper, J. A., Jenkins, R. G. & Hatley, R. J. D. Emerging therapeutic opportunities for integrin inhibitors. *Nat. Rev. Drug Discov.* **21**, 60–78 (2022).
19. Pawlak, M. R. *et al.* RAD-TGTs: high-throughput measurement of cellular mechanotype via rupture and delivery of DNA tension probes. *Nat. Commun.* **14**, 2468 (2023).
20. Yang, S. *et al.* DNA-functionalized artificial mechanoreceptor for de novo force-responsive signaling. *Nat. Chem. Biol.* **20**, 1066–1077 (2024).
21. Duan, Y. *et al.* Mechanically triggered hybridization chain reaction. *Angew. Chem. Int. Ed.* **60**, 19974–19981 (2021).
22. Morsut, L. *et al.* Engineering customized cell sensing and response behaviors using synthetic Notch receptors. *Cell* **164**, 780–791 (2016).
23. Langridge, P. D. & Struhl, G. Epsin-dependent ligand endocytosis activates Notch by force. *Cell* **171**, 1383-1396.e12 (2017).
24. Stabley, D. R., Jurchenko, C., Marshall, S. S. & Salaita, K. S. Visualizing mechanical tension across membrane receptors with a fluorescent sensor. *Nat. Methods* **9**, 64–67 (2012).
25. Sun, M., Deng, J. & Walther, A. Communication and cross-regulation between chemically fueled sender and receiver reaction networks. *Angew. Chem. Int. Ed.* **62**, e202214499 (2023).
26. Deng, J. & Walther, A. Autonomous DNA nanostructures instructed by hierarchically concatenated chemical reaction networks. *Nat. Commun.* **12**, 5132 (2021).
27. Sharma, C., Samanta, A., Schmidt, R. S. & Walther, A. DNA-based signaling networks for transient colloidal co-assemblies. *J. Am. Chem. Soc.* **145**, 17819–17830 (2023).
28. Ma, Y. *et al.* Advancing targeted combination chemotherapy in triple negative breast cancer: nucleolin aptamer-mediated controlled drug release. *J. Transl. Med.* **22**, 604 (2024).
29. Choo, P., Liu, T. & Odom, T. W. Nanoparticle shape determines dynamics of targeting nanoconstructs on cell membranes. *J. Am. Chem. Soc.* **143**, 4550–4555 (2021).
30. Liu, Y. *et al.* A non-G-quadruplex DNA aptamer targeting ncl for diagnosis and therapy in bladder cancer. *Adv. Healthc. Mater.* **12**, 2300791 (2023).
31. Jurchenko, C., Chang, Y., Narui, Y., Zhang, Y. & Salaita, K. S. Integrin-generated forces lead to streptavidin-biotin unbinding in cellular adhesions. *Biophys. J.* **106**, 1436–1446 (2014).
32. Jo, M. H. *et al.* Single-molecule characterization of subtype-specific β1 integrin mechanics. *Nat. Commun.* **13**, 7471 (2022).
33. Yin, J. *et al.* An intelligent DNA nanodevice for precision thrombolysis. *Nat. Mater.* **23**, 854–862 (2024).
34. Velusamy, A., Sharma, R., Rashid, S. A., Ogasawara, H. & Salaita, K. DNA mechanocapsules for programmable piconewton responsive drug delivery. *Nat. Commun.* **15**, 704 (2024).
35. Li, S. *et al.* A DNA nanorobot functions as a cancer therapeutic in response to a molecular trigger in vivo. *Nat. Biotechnol.* **36**, 258–264 (2018).
36. Di, Z. *et al.* An orthogonally regulatable DNA nanodevice for spatiotemporally controlled biorecognition and tumor treatment. *Sci. Adv.* **6**, eaba9381 (2020).
37. Tang, H. *et al.* Cholesterol modulates the physiological response to nanoparticles by changing the composition of protein corona. *Nat. Nanotechnol.* **18**, 1067–1077 (2023).
38. Wang, Z. *et al.* Organelle-specific triggered release of immunostimulatory oligonucleotides from intrinsically coordinated DNA–metal–organic frameworks with soluble exoskeleton. *J. Am. Chem. Soc.* **139**, 15784–15791 (2017).
39. Commisso, C. *et al.* Macropinocytosis of protein is an amino acid supply route in Ras-transformed cells. *Nature* **497**, 633–637 (2013).
40. Kotula, J. W. *et al.* Aptamer-mediated delivery of splice-switching oligonucleotides to the nuclei of cancer cells. *Nucl. Acid Ther.* **22**, 187–195 (2012).

41. Koutsioumpa, M. *et al.* Interplay between αvβ3 integrin and nucleolin regulates human endothelial and glioma cell migration. *J. Biol. Chem.* **288**, 343–354 (2013).
42. Song, N. *et al.* The nuclear translocation of endostatin is mediated by its receptor nucleolin in endothelial cells. *Angiogenesis* **15**, 697–711 (2012).
43. Bi, J. *et al.* Identification of nucleolin as a lipid-raft-dependent β1-integrin-interacting protein in A375 cell migration. *Mol. Cells* **36**, 507–517 (2013).
44. Ding, Y. *et al.* Heat shock cognate 70 regulates the translocation and angiogenic function of nucleolin. *Arterioscler. Thromb. Vasc. Biol.* **32**, e126–e134 (2012).
45. Huang, Y. *et al.* The angiogenic function of nucleolin is mediated by vascular endothelial growth factor and nonmuscle myosin. *Blood* **107**, 3564–3571 (2006).
46. Kechagia, Z. *et al.* The laminin–keratin link shields the nucleus from mechanical deformation and signalling. *Nat. Mater.* **22**, 1409–1420 (2023).
47. Rennick, J. J., Johnston, A. P. R. & Parton, R. G. Key principles and methods for studying the endocytosis of biological and nanoparticle therapeutics. *Nat. Nanotechnol.* **16**, 266–276 (2021).
48. Schink, K. O. *et al.* The phosphoinositide coincidence detector Phafin2 promotes macropinocytosis by coordinating actin organisation at forming macropinosomes. *Nat. Commun.* **12**, 6577 (2021).
49. Mercer, J. & Helenius, A. Virus entry by macropinocytosis. *Nat. Cell Biol.* **11**, 510–520 (2009).
50. Swanson, J. A. Shaping cups into phagosomes and macropinosomes. *Nat. Rev. Mol. Cell Biol.* **9**, 639–649 (2008).
51. Quinn, S. E. *et al.* The structural dynamics of macropinosome formation and PI3-kinase-mediated sealing revealed by lattice light sheet microscopy. *Nat. Commun.* **12**, 4838 (2021).
52. Rohatgi, R. *et al.* The interaction between N-WASP and the Arp2/3 complex links Cdc42-dependent signals to actin assembly. *Cell* **97**, 221–231 (1999).
53. Kundu, S., Pal, K., Pyne, A. & Wang, X. Force-bearing phagocytic adhesion rings mediate the phagocytosis of surface-bound particles. *Nat. Commun.* **16**, 984 (2025).
54. Prehoda, K. E., Scott, J. A., Mullins, R. D. & Lim, W. A. Integration of multiple signals through cooperative regulation of the N-WASP-Arp2/3 complex. *Science* **290**, 801–806 (2000).
55. Du, Y. *et al.* Ligand dilution analysis facilitates aptamer binding characterization at the single-molecule level. *Angew. Chem. Int. Ed.* **135**, e202215387 (2023).
56. Ferreira, C. S. M., Matthews, C. S. & Missailidis, S. DNA aptamers that bind to MUC1 tumour marker: Design and characterization of MUC1-binding single-stranded DNA aptamers. *Tumor Biol.* **27**, 289–301 (2006).
57. Song, Y. *et al.* Selection of DNA aptamers against epithelial cell adhesion molecule for cancer cell imaging and circulating tumor cell capture. *Anal. Chem.* **85**, 4141–4149 (2013).
58. Singuru, M. M. R., Amouzadeh Tabrizi, M., Bhattacharyya, P., Ali, A. A. & You, M. Force-responsive delivery of anticancer drugs via a DNA mechanical nanovehicle. *Nano Lett.* **25**, 336–342 (2025).
59. Ma, V. P. *et al.* Mechanically induced catalytic amplification reaction for readout of receptor-mediated cellular forces. *Angew. Chem. Int. Ed.* **128**, 5578–5582 (2016).
60. Heljasvaara, R. *et al.* Generation of biologically active endostatin fragments from human collagen XVIII by distinct matrix metalloproteases. *Exp. Cell Res.* **307**, 292–304 (2005).
61. Shi, H. *et al.* Nucleolin is a receptor that mediates antiangiogenic and antitumor activity of endostatin. *Blood* **110**, 2899–2906 (2007).
62. Wang, D. *et al.* Enrichment and sensing tumor cells by embedded immunomodulatory DNA hydrogel to inhibit postoperative tumor recurrence. *Nat. Commun.* **14**, 4511 (2023).
63. Li, Y. *et al.* Covalent LYTAC enabled by DNA aptamers for immune checkpoint degradation therapy. *J. Am. Chem. Soc.* **145**, 24506–24521 (2023).
64. Zhou, J. & Rossi, J. Aptamers as targeted therapeutics: current potential and challenges. *Nat. Rev. Drug. Discov.* **16**, 181–202 (2017).
65. Kim, S. H. & Li, I. T. S. Altering cell junctional tension in spheroids through E-cadherin engagement modulation. *ACS Appl. Bio Mater.* **7**, 3766–3776 (2024).
66. Zhao, Y., Sarkar, A. & Wang, X. Peptide nucleic acid based tension sensor for cellular force imaging with strong DNase resistance. *Biosens. Bioelectron.* **150**, 111959 (2020).

770 67. Rashid, S. A. *et al.* Nuclease-resistant and hydrogel-tethered DNA hairpin probes map pN cell traction
771 forces. *ACS Appl. Mater. Interfaces* **15**, 33362–33372 (2023).
772 68. Sethi, S. *et al.* Nuclease-resistant L-DNA tension probes enable long-term force mapping of single cells and
773 cell consortia. *Angew. Chem. Int. Ed.* **63**, e202413983 (2024).
774 69. Peng, Y.-H. *et al.* Dynamic matrices with DNA-encoded viscoelasticity for cell and organoid culture. *Nat.*
775 *Nanotechnol.* **18**, 1463–1473 (2023).
776 70. Zhang, H., Kim, S. H. & Li, I. T. S. Decoy DNA protects molecular tension probes from DNase degradation.
777 *Angew. Chem. Int. Ed.* e202506590 (2025).
778 71. Samanta, A., Baranda Pellejero, L., Masukawa, M. & Walther, A. DNA-empowered synthetic cells as
779 minimalistic life forms. *Nat. Rev. Chem.* **8**, 454–470 (2024).
780 72. Galush, W. J., Nye, J. A. & Groves, J. T. Quantitative fluorescence microscopy using supported lipid bilayer
781 standards. *Biophys. J.* **95**, 2512–2519 (2008).
782 73. Case, L. B., De Pasquale, M., Henry, L. & Rosen, M. K. Synergistic phase separation of two pathways
783 promotes integrin clustering and nascent adhesion formation. *eLife* **11**, e72588 (2022).
784